Editors' Suggestion

Blue-Detuned Magneto-optical Trap of CaF Molecules

Samuel J. Li,[1,*] Connor M. Holland,[1,*] Yukai Lu,[1,2] and Lawrence W. Cheuk[1,†]
[1]Department of Physics, Princeton University, Princeton, New Jersey 08544, USA
[2]Department of Electrical and Computer Engineering, Princeton University, Princeton, New Jersey 08544, USA

(Received 9 November 2023; accepted 14 May 2024; published 6 June 2024)

A key method to produce trapped and laser-cooled molecules is the magneto-optical trap (MOT), which is conventionally created using light red detuned from an optical transition. In this work, we report a MOT for CaF molecules created using blue-detuned light. The blue-detuned MOT (BDM) achieves temperatures well below the Doppler limit and provides the highest densities and phase-space densities reported to date in CaF MOTs. Our results suggest that BDMs are likely achievable in many relatively light molecules including polyatomic ones, but our measurements suggest that BDMs will be challenging to realize in substantially heavier molecules due to sub-mK trap depths. In addition to record temperatures and densities, we find that the BDM substantially simplifies and enhances the loading of molecules into optical tweezer arrays, which are a promising platform for quantum simulation and quantum information processing. Notably, the BDM reduces molecular number requirements ninefold compared to a conventional red-detuned MOT, while not requiring additional hardware. Our work therefore substantially simplifies preparing large-scale molecular tweezer arrays, which are a novel platform for simulation of quantum many-body dynamics and quantum information processing with molecular qubits.

DOI: 10.1103/PhysRevLett.132.233402

Laser-cooled molecules are a promising platform for quantum simulation, quantum information processing, studies of ultracold molecular collisions, and precision probes of physics beyond the standard model [1–4]. A workhorse technology for producing trapped laser-cooled atoms and molecules is the magneto-optical trap (MOT), where a magnetic gradient in combination with near-resonant light provides both cooling and spatial confinement. Conventionally, MOTs are created using light red detuned from an optical transition. They rely on Doppler cooling and achieve temperatures near the Doppler limit $T_D = \hbar\Gamma/(2k_B)$, where Γ is the excited state linewidth.

Starting with the first molecular MOTs of SrF [5,6], MOTs have been demonstrated for many diatomic and polyatomic molecules [7–10]. These developments have enabled conservative optical and magnetic trapping [11–15] that has allowed coherent control of rotational states [11], exploration of ultracold molecular collisions [16–18], and creation of arrays of single molecules held in programmable tweezer traps [19,20]. Notably, because of microscopic detection and control capabilities, these molecular tweezer arrays have emerged as a promising platform for simulating interacting quantum spin models and realizing quantum circuits. In these arrays, although the crucial building blocks of coherent electric dipolar interactions and entangling two-qubit gates have been demonstrated recently [21,22], efficient tweezer loading remains an experimental challenge because of low molecular MOT densities. While density enhancement techniques such as laser cooling in optical traps [12,13,23,24] and optical compression [25] help, they come at a cost of increased experimental complexity. Simple techniques that create substantially denser MOTs are therefore of practical utility.

In this work, we demonstrate a blue-detuned MOT (BDM) for CaF molecules that produces record cold temperatures well below the Doppler limit, and high densities. Practically, we find that the BDM substantially enhances the loading of molecular tweezer arrays when compared to a conventional red-detuned MOT, which effectively reduces initial MOT number requirements ninefold. Notably, the BDM is simple to implement and only uses hardware that is already needed for a red MOT.

In molecular MOTs, optical cycling is achieved by addressing a rotational-lowering transition [26] (e.g., $N = 1 \rightarrow N' = 0$ transition, where N denotes the rotational quantum number). In these so-called type-II systems, the number of excited states is less than or equal to the number of ground states. As pointed out in [27], with red-detuned light, type-II systems experience Doppler cooling at high velocities and sub-Doppler heating at low velocities. With blue-detuned light, Doppler heating and sub-Doppler cooling occur instead [7,13,23,24,27]. It was subsequently realized that blue-detuned MOTs, which offer spatial confinement in addition to sub-Doppler cooling, are possible [28–30]. The first BDM was realized with Rb atoms [28]; recently, molecular BDMs of YO [31] and SrF [18] have been created.

To create a blue-detuned CaF MOT, we start with a red-detuned MOT formed using a dc quadrupolar magnetic field (symmetry axis along $\hat{z}$) and light red detuned from the

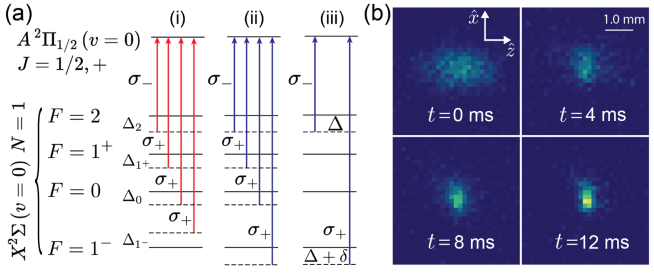

FIG. 1. MOT laser configurations and Λ-BDM loading dynamics. (a) Laser configurations for (i) a red-detuned dc MOT, (ii) the four-frequency BDM, and (iii) the two-frequency Λ-BDM. The single-photon (two-photon) frequency detuning is denoted Δ (δ). See Ref. [32] for specific detunings and intensities. The hyperfine splittings from top to bottom are 25, 47, and 76 MHz. (b) *In situ* images of a Λ-BDM at time t following direct loading from a Λ-cooled cloud ($B'_z = 27$ G/cm).

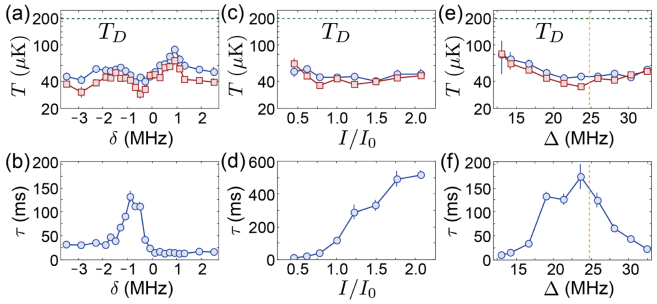

FIG. 2. Parameter dependences of the Λ-BDM temperature T and lifetime τ. (a),(b) T and τ versus two-photon detuning δ, with $\Delta = 23.8$ MHz and $I = 5.8(2)$ mW/cm^2. (c),(d) T and τ versus the intensity I/I_0 per beam [$I_0 = 5.8(2)$ mW/cm^2, $\Delta = 23.8$ MHz, $\delta = -0.7$ MHz]. (e),(f) T and τ versus single-photon detuning Δ [$\delta = -0.7$ MHz, $I = 5.8(2)$ mW/cm^2]. The vertical dashed line shows the value of Δ where the $F = 2$ frequency component is resonant with the $F = 1^+$ manifold. In (a),(c),(e), axial (radial) temperatures T_z (T_r) are shown in blue circles (red squares) and the horizontal dashed line shows the Doppler temperature T_D. For all plots, $B'_z = 10.4$ G/cm.

$X^2\Sigma(N=1) \rightarrow A^2\Pi_{1/2}(J=1/2,+)$ transition. The cooling light is sent along three orthogonal directions and consists of four frequency components nominally addressing the four ground hyperfine manifolds [Fig. 1(a)(i)]. After initial capture of molecules from a cryogenic buffer gas beam, the red-detuned MOT is magnetically compressed [11,25], reaching a mean Gaussian width of $\sigma = 680(30)$ μm and a temperature of $T = 3.9(4)$ mK.

Since BDMs have low capture velocities [27–30], we further precool the molecules in free space with Λ-enhanced gray molasses cooling to ∼10 μK before loading into a BDM [18,23,31]. The sample expands negligibly during this stage and 49(1)% remains.

We next transfer molecules into a BDM with four frequency components, operating at a detuning of $\approx +20$ MHz and a gradient of $B'_z = 14.6$ G/cm (details in [32]). At optimal parameters, ≈70% is transferred. Notably, the BDM rapidly approaches equilibrium over a $1/e$ time of 7.9(4) ms. The equilibrium axial (radial) Gaussian width is $\sigma_z = 294(2)$ μm [$\sigma_r = 215(2)$ μm], and the axial (radial) temperature is $T_z = 195(5)$ μK [$T_r = 186(12)$ μK]. The corresponding mean size is $\sigma = \sigma_r^{2/3}\sigma_z^{1/3} = 239(2)$ μm and mean temperature is $T = T_r^{2/3}T_z^{1/3} = 189(8)$ μK, around the Doppler limit of $T_D = 200$ μK. The equilibration time is similar to that reported for SrF and is significantly faster than observed in YO (∼50 ms). We attribute the rapid equilibration to the high photon scattering rate of $\Gamma_{sc} = 2.0(2) \times 10^6$ s^{-1} [32]. Although this provides large trapping and damping forces, it limits the achievable temperature.

To cool further, we use a two-frequency configuration [Fig. 1(a)(iii)] with light addressing the highest ($J = 3/2$, $F = 2$) and lowest ($J = 1/2, F = 1^-$) hyperfine manifolds. This configuration, which we call the Λ-BDM, is similar to that used in Λ cooling, where velocity-dependent coherent dark states enable cooling to sub-Doppler temperatures. Similar to the four-frequency BDM, the equilibrium size is reached rapidly over several milliseconds [Fig. 1(b)].

To characterize the Λ-BDM, we investigate its temperature (T) and lifetime (τ) dependences on the single-photon frequency detuning (Δ), two-photon frequency detuning (δ), and intensity (I). First, we fix the gradient at $B'_z = 10.4$ G/cm and probe the dependences of T and τ on δ. We observe a temperature minimum and lifetime maximum near two-photon resonance ($\delta = 0$), with a striking rise in temperature and decrease in lifetime for $\delta > 0$ [Figs. 2(a) and 2(b)]. These features are similar to those observed in free-space Λ cooling [23] and in a BDM of YO [31], indicating the presence of velocity-dependent coherent dark states. Notably, at $B'_z = 10.4$ G/cm and $\delta = -0.7$ MHz, we obtain a temperature of $T = 36.7(2)$ μK, 5 times below the Doppler limit of $T_D = 200$ μK [Fig. 2(a)].

We next explore the dependences of T and τ on the light intensity I. Similar to free-space Λ cooling [23], the robustness of the dark states increases with intensity due to increased two-photon coupling. Because the two-photon resonance varies across the BDM due to the magnetic gradient, one expects that a minimum intensity is needed to counteract magnetic broadening. However, at high intensities, photon scattering is increased and leads to higher temperatures. There is therefore an optimal intensity for reaching the lowest temperatures, which we indeed observe [Figs. 2(c) and 2(d)]. Notably, we find that the lifetime improves with intensity at the expense of higher temperatures. As a compromise, we operate at $I = I_0 = 5.8(2)$ mW/cm^2.

Similar to the dependence on I, we expect an optimum in the single-photon detuning Δ. The optimum occurs

as a balance between increased off-resonant scattering at small Δ and decreased two-photon coupling at large Δ, which reduces the robustness of coherent dark states [23]. Fixing $I = 5.8(2)$ mW/cm^2 and $\delta = -0.7$ MHz, we find an optimum of $\Delta \approx 24$ MHz [Figs. 2(e) and 2(f)]. With optimized parameters ($\Delta = 23.8$ MHz, $\delta = -0.7$ MHz, $I = 5.8(2)$ mW/cm^2), we measure a scattering rate of $\Gamma_{sc} = 0.65(19) \times 10^6$ s^{-1} [32], substantially lower than the four-frequency BDM, but much higher than free-space Λ cooling [23].

Motivated by the practical objective of increasing molecular densities, we next explore the dependence of the Λ-BDM on magnetic gradient B'_z. In red-detuned MOTs, a strategy to increase density is magnetic compression through increasing B'_z [37]. At a fixed temperature T, the MOT size decreases as $1/\sqrt{B'_z}$. Consequently, the density rises as $B'^{3/2}_z$ [32,37]. In detail, the MOT can be modeled with an equation of motion containing a restoring force and velocity damping: $\ddot{x} = -\alpha(x)\dot{x} + F(x)/m$ [5,8,31,37]. Near the MOT center and at low velocities, the damping coefficient α is approximately constant, and the restoring force is approximated by Hooke's law $F(x) = -kx$, where k is the spring constant. The restoring force arises from magnetic-field dependent light scattering. Therefore, F is a function of the local magnetic field B. At the center of a quadrupole field in a MOT, $F(x) = F(B(x)) \approx B'x(dF/dB)$. Hence, near the MOT center, $k \propto B'_z$. Using a generalized Virial theorem that equates potential and kinetic energies [32], one finds that $\sigma \propto 1/\sqrt{B'_z}$ and the density grows as $(B'_z)^{3/2}$ at a fixed T.

Figure 3 shows the observed dependence of the size (σ), temperature (T), and lifetime (τ) versus B'_z. We find that σ scales as $1/\sqrt{B'_z}$ up to ≈20 G/cm [Fig. 3(a)]. T increases slightly with gradient, but remains well below T_D even up to 40 G/cm [Fig. 3(b)]. The rising temperature is likely because the mean magnetic field experienced by the molecules rises as $\sqrt{B'_z}$ [32], which in turn perturbs the coherent dark states responsible for sub-Doppler cooling. Notably, τ decreases significantly starting at $B'_z \approx 15$ G/cm [Fig. 3(c)]. At 30 G/cm, τ becomes comparable to the equilibration timescale. Density enhancement via further magnetic compression is therefore not a viable method for our BDM, and the optimal gradient is a compromise between minimizing σ and T and maximizing τ.

Empirically, the smallest sizes occur at $B'_z = 27$ G/cm [$\sigma = 172(4)$ μm, $T = 60(4)$ μK], the lowest temperatures at $B'_z = 6.2$ G/cm [$\sigma = 277(5)$ μm, $T = 31(1)$ μK], and the highest peak phase space density (PSD) at $B'_z = 14.6$ G/cm [$\sigma = 188(3)$ μm, $T = 39(2)$ μK]. At optimal parameters and with $N = 6.2(15) \times 10^3$ molecules in the Λ-BDM, we obtain a peak density of $n_0 = 7(2) \times 10^7$ cm^{-3} and a peak PSD of $3.0(8) \times 10^{-9}$. Compared to the compressed red-detuned MOT, these values correspond to a density improvement of 19(3) and a PSD enhancement of $1.6(3) \times 10^4$. Notably, by applying free-space Λ cooling to a cloud released from a Λ-BDM ($B'_z = 18.7$ G/cm), we obtain a peak PSD of $2.3(6) \times 10^{-8}$ [$\sigma = 182(2)$ μm, $T = 10.6(6)$ μK], the highest reported to date for CaF in free space.

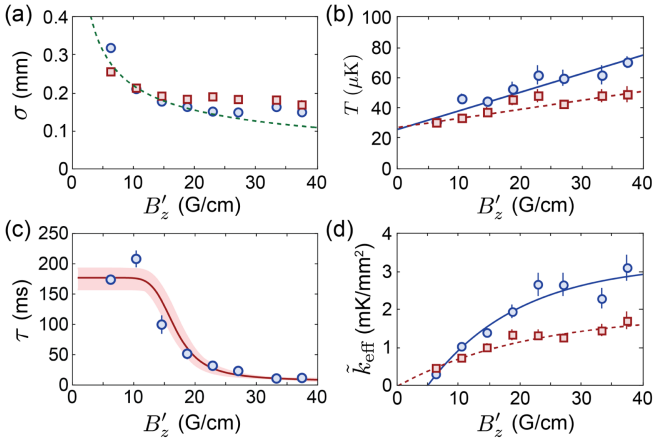

FIG. 3. Λ-BDM properties versus axial magnetic gradient B'_z. (a) Gaussian axial (radial) width σ_z (σ_r) shown in blue circles (red squares). Green dashed line shows a fit of the mean size $\sigma = \sigma_r^{2/3}\sigma_z^{1/3}$ to $1/B_z^{1/2}$ for data up to 20 G/cm. (b) Axial (radial) temperature T_z (T_r) shown in blue circles (red squares). The blue solid (red dashed) line is a linear fit of the axial (radial) temperature. (c) Lifetime τ (blue circles) versus B'_z. Solid line shows a fit to the loss model described in the main text that uses the measured MOT damping forces, restoring forces, temperatures, and sizes [32]. The shaded regions are uncertainty bands from 1σ uncertainties of fitted parameters [32]. (d) Effective spring constant $\tilde{k}_{\text{eff}} = T/\sigma^2$ for the axial (radial) direction shown in blue circles (red squares). The blue solid (red dashed) line is a fit of the axial (radial) data to an exponential saturation curve. The axial fit includes a horizontal offset to phenomenologically capture the effect of gravity, which is along $\hat{z}$.

To investigate the origin of the short lifetimes at high gradients, we examine the dependence of the restoring force on B'_z, since an insufficient restoring force could lead to loss. Assuming Hooke's law and constant velocity damping, the spring constant k can be obtained from T and σ via $k_{\text{eff}} = k_B T/\sigma^2$ [32]. In Fig. 3(d), we show $\tilde{k}_{\text{eff}} = k_{\text{eff}}/k_B$ versus B'_z for both the radial and axial directions. At gradients below $B'_z \approx 10$ G/cm, $\tilde{k}_{\text{eff}}$ is linear in B'_z, as expected, with values similar to those reported for YO [31]. At higher gradients, $\tilde{k}_{\text{eff}}$ appears to saturate, indicating that the restoring force decreases. Because molecules experience an average magnetic field that grows as $\sqrt{B'_z}$, the saturation of $\tilde{k}_{\text{eff}}$ suggests that $F(B)$ is substantially sublinear at higher magnetic fields.

To test this hypothesis, we directly measure $F(B)$. We create dense and cold samples by loading a Λ-BDM and subsequently applying free-space Λ cooling. We then impart an initial radial velocity of $v_0 \approx 200$ mm/s by

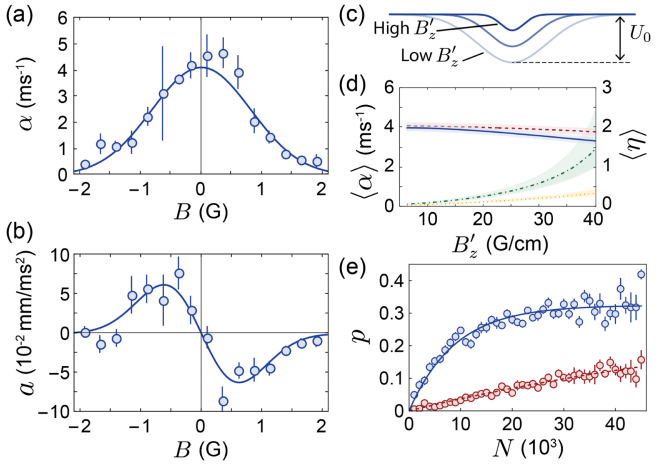

FIG. 4. Velocity damping, restoring force, and enhanced tweezer loading. (a) Damping constant α versus magnetic field B. Solid blue line shows a Gaussian fit. (b) Acceleration $a(B)$ versus B. Solid line is a fit to the derivative of a Gaussian. (c) Illustration showing decreasing trap depths U_0 and trap sizes d with increasing magnetic gradient B'_z. Both U_0 and d scale as $1/B'_z$. (d) Simulated average damping $\langle\alpha\rangle$ and temperature to trap depth ratio $\langle\eta\rangle$, versus magnetic gradient B'_z. $\langle\alpha\rangle$ for the axial (radial) directions are shown by the blue solid (red dashed) line; $\langle\eta\rangle$ for the axial (radial) directions are shown by the green solid (orange dashed) line. (e) Tweezer loading probability p versus initial MOT number N. Solid blue (dashed red) line is an exponential fit to data with (without) using a BDM.

pulsing on a beam resonant with the $X^2\Sigma(N=1) \rightarrow B^2\Sigma(N=0)$ transition. We next apply a uniform magnetic field $\vec{B}$ along the push direction ($\vec{B} \| \vec{v}_0$) and switch on Λ-BDM light for a variable duration t. At each t, we measure the velocity v via time-of-flight expansion. By fitting to $v(t) = Ae^{-\alpha t} + v_\infty$, we extract the damping coefficient α and the terminal velocity v_∞. The restoring force $F(B)$ is then obtained via $F = m\alpha v_\infty$. To determine v_∞ more accurately, we perform a second set of measurements where the push beam is not applied and the molecules start with $v_0 = 0$ [32].

Figures 4(a) and 4(b) show the extracted damping curve $\alpha(B)$ and acceleration curve $a(B) = F(B)/m$. For $a(B)$, we observe the expected sign change upon reversing B. We also find that $\alpha(B)$ and $a(B)$ are significant only when $|B| < 1$ G. Furthermore, the restoring force is approximately linear only for $|B| < 0.5$ G. At $B'_z = 20$ G/cm, this corresponds to a radial size of 0.5 mm.

The acceleration curve $a(B)$ explains why short lifetimes are observed at high gradients. In short, we find that the effective BDM trap depth becomes comparable to the molecular temperatures, leading to loss. Using $a(B)$, we define an effective conservative trapping potential $U(x) = -m\int a(B(x))dx$ along the radial and axial directions [38]. It follows that both the spatial scale and the magnitude of $U(x)$ scale inversely with B'_z [Fig. 4(c)]. That is, both the trap size and depth decrease with B'_z. Assuming $U(x)$ is Gaussian, given by $U(x) = -U_0 \exp[-x^2/(2d^2)]$, we obtain a trap depth of $U_0(B'_z) = k_B \times 4.6(10)$ mK(G/cm)$/B'_z$ and a trap size of $d(B'_z) = 0.62(4)$ G$/B'_z$. Notably, at a typical gradient of 20 G/cm, $U_0 = k_B \times 230(50)$ μK, which is only 4 times higher than the observed temperature. These trap depths are much smaller than the ∼50 mK depths reported for red-detuned molecular MOTs [6,29,37] and ∼0.5 K depths reported for red-detuned atomic MOTs [39].

To further support our hypothesis that short lifetimes arise from low trap depths, we quantitatively examine both the trap-averaged damping constant $\langle\alpha\rangle$ and the temperature to trap depth ratio $\langle\eta\rangle = \langle(k_B T)/U(x)\rangle$. Monte Carlo simulations using measured curves of $\alpha(B)$ and $a(B)$ show that $\langle\alpha\rangle$, which determines the average cooling rate, varies by no more than 20% over experimentally relevant gradients. On the other hand, $\langle\eta\rangle$ varies significantly and even exceeds unity. Because the molecular fraction above the local trap depth is given by $\exp(-1/\eta)$, this confirms that a shallow trap depth, rather than a lack of velocity damping, is the primary loss mechanism at high gradients. Simulations using a loss model incorporating α and η also agree with the data within experimental uncertainty [Fig. 3(c)], confirming our hypothesis [32]. Our identification of shallow trap depths at high magnetic gradients has implications for extending BDMs to other molecular species. In particular, because a minimum gradient is needed to counteract gravity, BDMs could be challenging to implement for much heavier molecules. Specifically, BDMs of molecular species with mass > 1000 amu and similar optical properties are likely not possible.

Lastly, to demonstrate a key practical benefit of our work, we compare the loading of an optical tweezer array using a Λ-BDM versus using only a red-detuned MOT. In both cases, the molecules are transferred into an intermediate optical dipole trap (ODT), and then into tweezers with the aid of Λ cooling, where the final tweezer occupations are determined by fluorescent imaging [32]. By examining the tweezer loading probability p versus initial MOT number [Fig. 4(e)], we find that the Λ-BDM reduces the required molecule number by a factor of 9.3(8). Notably, the BDM allows saturated loading ($p \approx 0.35$ [22]) robustly over a wide range of experimentally accessible initial MOT numbers. It also significantly outperforms optical compression [25] robustly and without requiring additional hardware. Notably, dynamical optical compression used in [25] increased ODT numbers by ≈2 compared to using a red-detuned MOT alone. For tweezer loading, this directly reduces initial MOT number requirements by the same factor of 2, much lower than the factor of ≈9 achieved here with the Λ-BDM. Notably, our current work allows saturated tweezer loading, which opens the door to creating large molecular arrays needed to study quantum spin models in the many-body regime and quantum circuits with large arrays of molecular qubits.

In summary, we have demonstrated a blue-detuned MOT of CaF molecules that reaches record temperatures and densities. In addition, we demonstrate that Λ-BDMs significantly enhance loading of molecular tweezer arrays, a promising platform for quantum science [1–4,21,22]. Notably, since BDMs do not require additional experimental hardware beyond that needed in a conventional MOT, they are of great practical utility. In addition to enhanced tweezer loading, the higher densities in a BDM could aid studies of ultracold molecular collisions [16,18] and provide improved starting conditions for evaporative cooling. Contextualizing our BDM results with those reported recently for YO [31] and SrF [18], we observe that despite different spin rotation and hyperfine structure, a CaF BDM is also possible. This lends further support that BDMs could be widely applicable to other laser-coolable molecules, including polyatomic ones such as CaOH and SrOH [10,40–42]. Nevertheless, our work has revealed that extension of BDMs to much heavier molecules could be challenging because of limited trap depths.

We thank Callum Welsh for a careful reading of the manuscript. This work is supported by the National Science Foundation under Grant No. 2207518. S. J. L. acknowledges support from a Princeton Quantum Initiative Graduate Student Fellowship. C. M. H. acknowledges support from a Joseph Taylor Graduate Student Fellowship. L. W. C. acknowledges support from an Alfred P. Sloan Foundation under Grant No. FG-2022-19104.

*These authors contributed equally to this work.
†lcheuk@princeton.edu

[1] D. DeMille, Phys. Rev. Lett. **88**, 067901 (2002).
[2] L. D. Carr, D. DeMille, R. V. Krems, and J. Ye, New J. Phys. **11**, 055049 (2009).
[3] J. L. Bohn, A. M. Rey, and J. Ye, Science **357**, 1002 (2017).
[4] J. A. Blackmore, L. Caldwell, P. D. Gregory, E. M. Bridge, R. Sawant, J. Aldegunde, J. Mur-Petit, D. Jaksch, J. M. Hutson, B. Sauer *et al.*, Quantum Sci. Technol. **4**, 014010 (2018).
[5] J. F. Barry, D. J. McCarron, E. B. Norrgard, M. H. Steinecker, and D. DeMille, Nature (London) **512**, 286 (2014).
[6] D. J. McCarron, E. B. Norrgard, M. H. Steinecker, and D. DeMille, New J. Phys. **17**, 035014 (2015).
[7] S. Truppe, H. J. Williams, M. Hambach, L. Caldwell, N. J. Fitch, E. A. Hinds, B. E. Sauer, and M. R. Tarbutt, Nat. Phys. **13**, 1173 (2017).
[8] L. Anderegg, B. L. Augenbraun, E. Chae, B. Hemmerling, N. R. Hutzler, A. Ravi, A. Collopy, J. Ye, W. Ketterle, and J. M. Doyle, Phys. Rev. Lett. **119**, 103201 (2017).
[9] A. L. Collopy, S. Ding, Y. Wu, I. A. Finneran, L. Anderegg, B. L. Augenbraun, J. M. Doyle, and J. Ye, Phys. Rev. Lett. **121**, 213201 (2018).
[10] N. B. Vilas, C. Hallas, L. Anderegg, P. Robichaud, A. Winnicki, D. Mitra, and J. M. Doyle, Nature (London) **606**, 70 (2022).
[11] H. J. Williams, L. Caldwell, N. J. Fitch, S. Truppe, J. Rodewald, E. A. Hinds, B. E. Sauer, and M. R. Tarbutt, Phys. Rev. Lett. **120**, 163201 (2018).
[12] L. Anderegg, B. L. Augenbraun, Y. Bao, S. Burchesky, L. W. Cheuk, W. Ketterle, and J. M. Doyle, Nat. Phys. **14**, 890 (2018).
[13] T. K. Langin, V. Jorapur, Y. Zhu, Q. Wang, and D. DeMille, Phys. Rev. Lett. **127**, 163201 (2021).
[14] Y. Wu, J. J. Burau, K. Mehling, J. Ye, and S. Ding, Phys. Rev. Lett. **127**, 263201 (2021).
[15] L. Anderegg, N. B. Vilas, C. Hallas, P. Robichaud, A. Jadbabaie, J. M. Doyle, and N. R. Hutzler, Science **382**, 665 (2023).
[16] L. W. Cheuk, L. Anderegg, Y. Bao, S. Burchesky, S. S. Yu, W. Ketterle, K.-K. Ni, and J. M. Doyle, Phys. Rev. Lett. **125**, 043401 (2020).
[17] L. Anderegg, S. Burchesky, Y. Bao, S. S. Yu, T. Karman, E. Chae, K.-K. Ni, W. Ketterle, and J. M. Doyle, Science **373**, 779 (2021).
[18] V. Jorapur, T. K. Langin, Q. Wang, G. Zheng, and D. DeMille, Phys. Rev. Lett. **132**, 163403 (2024).
[19] L. Anderegg, L. W. Cheuk, Y. Bao, S. Burchesky, W. Ketterle, K.-K. Ni, and J. M. Doyle, Science **365**, 1156 (2019).
[20] C. M. Holland, Y. Lu, and L. W. Cheuk, Phys. Rev. Lett. **131**, 053202 (2023).
[21] C. M. Holland, Y. Lu, and L. W. Cheuk, Science **382**, 1143 (2023).
[22] Y. Bao, S. S. Yu, L. Anderegg, E. Chae, W. Ketterle, K.-K. Ni, and J. M. Doyle, Science **382**, 1138 (2023).
[23] L. W. Cheuk, L. Anderegg, B. L. Augenbraun, Y. Bao, S. Burchesky, W. Ketterle, and J. M. Doyle, Phys. Rev. Lett. **121**, 083201 (2018).
[24] S. Ding, Y. Wu, I. A. Finneran, J. J. Burau, and J. Ye, Phys. Rev. X **10**, 021049 (2020).
[25] Y. Lu, C. M. Holland, and L. W. Cheuk, Phys. Rev. Lett. **128**, 213201 (2022).
[26] B. K. Stuhl, B. C. Sawyer, D. Wang, and J. Ye, Phys. Rev. Lett. **101**, 243002 (2008).
[27] J. Devlin and M. Tarbutt, New J. Phys. **18**, 123017 (2016).
[28] K. N. Jarvis, J. A. Devlin, T. E. Wall, B. E. Sauer, and M. R. Tarbutt, Phys. Rev. Lett. **120**, 083201 (2018).
[29] T. K. Langin and D. DeMille, New J. Phys. **25**, 043005 (2023).
[30] S. Xu, P. Kaebert, M. Stepanova, T. Poll, M. Siercke, and S. Ospelkaus, Phys. Rev. Res. **4**, L042036 (2022).
[31] J. J. Burau, P. Aggarwal, K. Mehling, and J. Ye, Phys. Rev. Lett. **130**, 193401 (2023).
[32] See Supplemental Material at http://link.aps.org/supplemental/10.1103/PhysRevLett.132.233402 for experimental methods, measurement procedures, simulation information, supplemental data, and extended discussion, which includes Refs. [16,19–21,23,25,31,33–36].
[33] N. R. Hutzler, H.-I. Lu, and J. M. Doyle, Chem. Rev. **112**, 4803 (2012).
[34] S. Stenholm, Rev. Mod. Phys. **58**, 699 (1986).
[35] A. S. Parkins and P. Zoller, Phys. Rev. A **45**, 6522 (1992).
[36] J. A. Devlin and M. R. Tarbutt, Phys. Rev. A **98**, 063415 (2018).

[37] H. J. Williams, S. Truppe, M. Hambach, L. Caldwell, N. J. Fitch, E. A. Hinds, B. E. Sauer, and M. R. Tarbutt, New J. Phys. **19**, 113035 (2017).
[38] The restoring force is in general nonconservative, but it is conservative when restricted to the x-y plane ($z = 0$) or along the symmetry axis z.
[39] E. L. Raab, M. Prentiss, A. Cable, S. Chu, and D. E. Pritchard, Phys. Rev. Lett. **59**, 2631 (1987).
[40] L. Baum, N. B. Vilas, C. Hallas, B. L. Augenbraun, S. Raval, D. Mitra, and J. M. Doyle, Phys. Rev. Lett. **124**, 133201 (2020).
[41] I. Kozyryev, L. Baum, K. Matsuda, B. L. Augenbraun, L. Anderegg, A. P. Sedlack, and J. M. Doyle, Phys. Rev. Lett. **118**, 173201 (2017).
[42] D. Mitra, N. B. Vilas, C. Hallas, L. Anderegg, B. L. Augenbraun, L. Baum, C. Miller, S. Raval, and J. M. Doyle, Science **369**, 1366 (2020).